Separation and Purification Technology 378 (2025) 134664

Contents lists available at ScienceDirect

Separation and Purification Technology

journal homepage: www.elsevier.com/locate/seppur

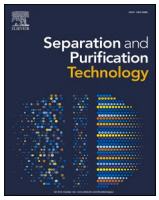

Optical coherence tomography for early detection, visualization and characterization of growth and deposition-driven scaling in reverse osmosis☆

Natalia Franco-Clavijo [a], Santiago Cespedes [a], Andreia Farinha [a,*], Geert-Jan Witkamp [a], Cristian Picioreanu [a], Johannes S. Vrouwenvelder [a,b], Bastiaan Blankert [a]

[a] King Abdullah University of Science and Technology (KAUST), Biological and Environmental Science and Engineering Division (BESE), Thuwal 23955-6900, Saudi Arabia
[b] Department of Biotechnology, Faculty of Applied Sciences, Delft University of Technology, Van der Maasweg 9, 2629 HZ Delft, The Netherlands

ARTICLE INFO

Editor: B. Van der Bruggen

Keywords:
Gypsum scaling
Desalination
Reverse osmosis
Crystal induction time
Membrane

ABSTRACT

Reverse osmosis (RO) desalination is the leading technology for industrial and municipal water production in water-stressed regions. While developing chemical-free scaling control strategies helps mitigate the environmental impact of brine discharge, it also increases the risk of membrane scaling due to high salt concentrations. Establishing methods for early detection and localization of scaling is essential, as well as understanding the impact on key operational parameters. This study evaluated optical coherence tomography (OCT) for real-time monitoring of growth- and deposition-driven gypsum fouling in RO systems. Membrane fouling simulators were operated under constant flux conditions using unsaturated and supersaturated synthetic water solutions. Real-time monitoring of operational parameters revealed that growth and deposition fouling had a greater impact on transmembrane pressure than pressure drop increase. OCT imaging visualized scaling progression, with optical and SEM imaging confirming distinct morphologies: sharp, translucent crystals in growth-driven scaling and a white, amorphous fouling layer in deposition. Data processing further provided quantitative assessment of area coverage and fouling volume, with membrane autopsy indicating higher porosity in the deposition case. Crystal detection from OCT imaging evidenced sensitivity for early-stage scaling detection. In the growth case, a strong correlation was observed between initial crystal formation and regions of maximum saturation index, as revealed by CFD with multicomponent solute transport simulations. The variation in induction time across detection methods highlights the importance of sensitivity of monitoring techniques, positioning OCT as a valuable tool for early scaling detection, before conventional indicators point out to significant scaling.

1. Introduction

Membrane-based seawater desalination has become the preferred technology for potable water production in water-stressed regions. Reverse osmosis (RO) spiral wound membrane is the leading desalination technology in industrial and municipal applications [1,2]. The current industrial seawater reverse osmosis (SWRO) process typically operates at a water recovery rate of 35 % to 45 %, producing a concentrated brine approximately 1.6–2 times more saline than the feed seawater [3]. An estimated 90.5 million m^3 of concentrated seawater is generated daily [4], and the global RO desalination capacity is continuously increasing.

The most common method for brine management in SWRO plants is surface water discharge because of economic considerations and the large brine volume. Brine usually contains other additives used to control biofouling (biocides) and scaling (antiscalants) [5]. Direct brine disposal into the sea has been associated with several environmental impacts at the discharge point, where variations in salinity, temperature, chemical composition, and the presence of ecologically harmful additives can disrupt local marine ecosystems [6].

Several approaches have been considered to mitigate the effects of brine discharge into the sea, including brine volume minimization (e.g.,

☆ This article is part of a special issue entitled: 'EuroMembrane 2024' published in Separation and Purification Technology.

* Corresponding author.
E-mail address: andreia.farinha@kaust.edu.sa (A. Farinha).

https://doi.org/10.1016/j.seppur.2025.134664
Received 26 March 2025; Received in revised form 4 August 2025; Accepted 5 August 2025
Available online 6 August 2025

zero liquid discharge ZLD, minimum liquid discharge MLD) and reuse (metals recovery). While promising results have been achieved on a small scale, further research is needed to evaluate the feasibility of brine treatment in commercial seawater desalination plants [3,7,8]. Furthermore, reducing the brine volume by abstracting water will not reduce the environmental impact. Alternative strategies like blending brine with intake water, reduce the local effect of salinity, and avoiding the dosage of chemicals minimize the negative impacts of chemical additives [6,9]. Application of these strategies induce a high risk of membrane scaling due to – on one hand – the high concentration of salts (ZLD/MLD) and – on the other hand – the potential elimination of chemical additions like antiscalants. Nevertheless, scale formation has always been a limitation in operating RO systems, leading to flux decline, membrane degradation, decreased production, and increased operational costs [10].

Scaling refers to the precipitation of retained salts that reach supersaturation near the outlet of the membrane system [11–13]. In industrial practice, scaling is managed primarily through pH correction (e.g., acidity), softening (e.g., ion removal), and dosing antiscalants (e.g., crystallization inhibitors) [14]. Various alternative strategies, like optimizing module design [15,16], membrane surface and material modification [17,18], promoting controlled crystallization [16,19,20], have been considered, but have not been widely implemented or technologically developed.

Membrane scaling occurs through two pathways: bulk crystallization and surface crystallization. In bulk crystallization, mineral crystals form in solution via homogeneous nucleation or heterogeneous nucleation from impurities (e.g., particulates) and subsequently deposit onto the membrane, leading to cake formation. In contrast, surface crystallization occurs directly on the membrane through heterogeneous nucleation, resulting in surface blockage [21–25]. In large-scale RO membrane systems, these mechanisms often occur simultaneously, making it difficult to determine whether a crystal formed in the bulk solution or directly on the membrane surface [26]. While it is possible to distinguish where a crystal grows, nucleation origin remains uncertain. Despite advancements in scaling monitoring, further development is required to establish methods for early quantification and localization of scaling on RO feed channel, as well as to better understand the impact on key operational parameters.

Significant efforts have been dedicated to developing monitoring and controlling scaling strategies in the last three decades. External monitoring tools parallel to the RO plant have been proposed as early-warning systems [13,27]. For instance, an *ex-situ* scale observation detector (EXSOD) was developed for real-time optical monitoring of membrane scaling using high-resolution digital photography [28–30]. Although valuable results have been obtained, observations and data acquisition are limited during the early stages of scaling. More sensitive methods like ultrasonic time domain reflectometry (UTDR) and electrical impedance spectroscopy (EIS) have been implemented for *in-situ* scaling monitoring [31,32]. However, the physical quantities monitored in both UTDR and EIS do not directly measure scale-mass evolution on the membrane, which is particularly needed for modeling and predictions [33].

Optical coherence tomography (OCT) has proven to be a powerful tool for monitoring fouling development, evaluating spatial distribution, assessing cleaning efficiency, and supporting fouling characterization, modeling, and simulation, with data typically acquired for qualitative analysis of biofouling and operational performance [34–38]. In addition, OCT has been effectively used to monitor the formation of various types of scaling and has demonstrated its value in tracking scaling formation and crystal growth on desalination technologies like membrane distillation [39,40]. Therefore, OCT can potentially monitor scaling development through 2D and 3D imaging during RO operation, correlating the scale growth with operational indicators.

The objective of this study is to assess the potential of optical coherence tomography (OCT) as an imaging technique for monitoring and differentiating growth- and deposition-driven fouling in reverse osmosis systems. By integrating real-time operational parameter monitoring with OCT imaging and processing, the study aims to (i) investigate the impact of scaling on membrane performance, (ii) visualize and quantify scaling progression, and correlate with fluid dynamics / salt transport numerical simulations, (iii) discriminate crystal growth from deposition, (iv) evaluate OCT as an early detection tool for scaling.

2. Materials and methods

2.1. Setup

Membrane fouling simulators (MFS) used in this study were flow cells based on the design of Vrouwenvelder et al. [41]. The MFS consists of two stainless steel plates fastened with screws (tightened to 12–14 Nm). The top plate contains the feed channel (L: 20 cm, W: 4 cm, H: 711 μm) and three glass windows (diameter: 2 cm). The bottom plate contains the permeate channel (L: 20 cm, W: 4 cm, H: 250 μm). Commercially available feed and permeate spacers were used as harvested from a Dupont SW30HRLE4040 membrane filtration element. Membrane coupons were cut from a roll of pristine membrane (Dupont XLE) obtained directly from the manufacturer.

The experiments were conducted with two parallel systems, a system diagram is shown in Fig. 1. Each systems had a stirred feed-tank of 10 *L* (not shown in diagram), the volume was chosen relatively large, so that material deposited or precipitated onto the membrane would not affect the overall composition of the feed. Concentrate was recycled to the feed tank, while permeate was either recycled or abstracted. The feed flow was regulated to the setpoint v_{SP} by controlling a variable rate pump. The feed water temperature setpoint T_{SP} was maintained by measuring temperature at the discharge of the feed pump and controlled with a one-pass water chiller. The permeate flux setpoint J_{SP} was maintained by modifying the set-point of a pressure controller coupled to a pressure sensor. A differential pressure transmitter was used to monitor the pressure drop across the feed channel. Electrical conductivity was measured in both the concentrate and permeate streams. Depending on the experiment, a microfiltration unit (MF) was installed at the concentrate line to remove suspended solids.

2.2. Scaling experiments

The experiments were divided into three phases: compaction, conditioning, and scaling. Constant flux operation was employed throughout the experiments to ensure a stable concentration polarization profile during the initial stages of crystal growth. While operational modes in full-scale RO systems can vary depending on system configuration and demand, ranging from constant to variable average flux, constant flux was selected in the present study to provide a consistent and controlled framework for analyzing scaling behavior.

Membranes were compacted at 35 bar in solution for a minimum of 48 h until the flux stabilized within an acceptable range. During conditioning, the operation was changed to constant flux (25 L/m^2h) and constant nominal crossflow velocity (0.16 m/s) until a constant salt passage was observed (typically one week), with feed temperature regulated at 25.0 ± 0.5 °C. The selected permeate flux was based on the operational guidelines provided by the membrane manufacturer [14], while the chosen crossflow velocity falls within typical ranges reported in the literature for spiral-wound membrane systems [42,43]. After inducing scaling, the experiments were stopped when a maximum transmembrane pressure of ca. 35 bar was reached.

After each experiment, an autopsy was performed to collect fouled membrane samples. One sample was immersed in a 1 % HNO_3 solution and left to stir overnight, then cations in the solution were analyzed using Inductively Coupled Plasma Optical Emission Spectroscopy (ICP-OES, Agilent 5110, USA). A second fouled membrane coupon, along with a pristine membrane sample, were sputter-coated with a 5 nm

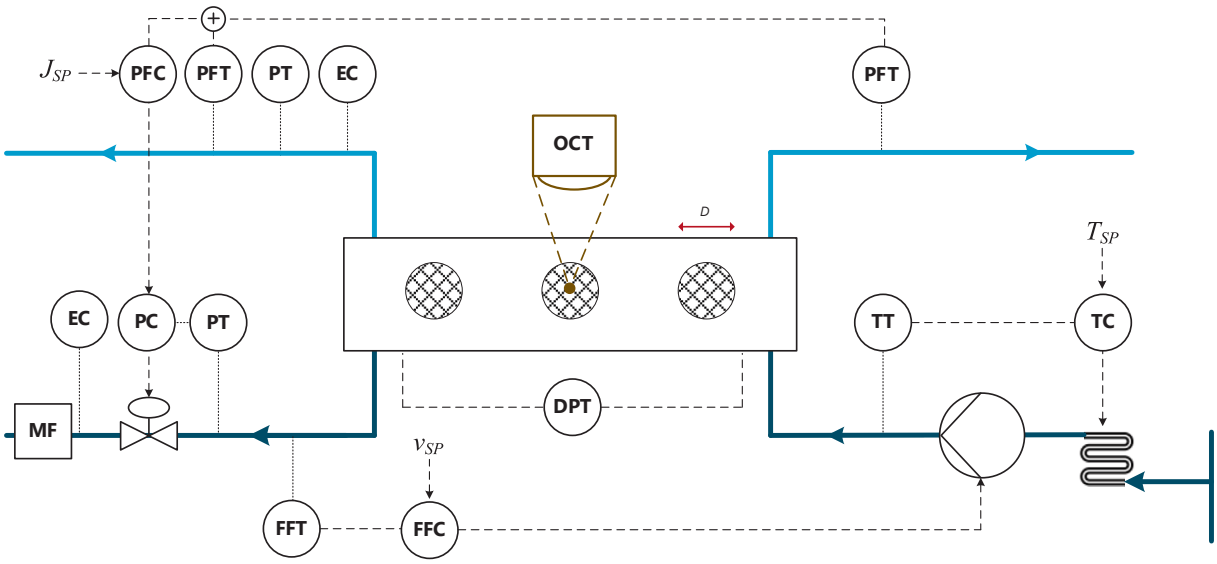

Fig. 1. Experimental setup for operation with a constant feed flow and permeate flux (adapted from [38]). The set points v_{SP}, T_{SP} and J_{SP}, refer to the crossflow velocity, feed temperature, and permeate flux, respectively. Feed water pump (MZR-11507-HS-F, HNP Mikrosysteme, Germany), feed mass flow transmitter (FFT) and controller (FFC) (CORI-FLOW™ M54, Bronkhorst, Netherlands), differential pressure transmitter (DPT) (Deltabar PMD75, Endress + Hauser, Switzerland), pressure transmitter (PT) and controller (PC) (EL-PRESS P502C, Bronkhorst, Netherlands), permeate mass flow transmitter (PFT) and controller (PFC) (mini CORI-FLOW™ M14, Bronkhorst, Netherlands), electrical conductivity meters (EC) (Cond 3310, WTW, Germany), chiller (AP15R-30-V12E VWR Nort America, USA). Microfiltration unit (MF) (housing 2.5″ × 10″, Simpure, USA, and polypropylene cartridge filter pore size 1 μm, Aquaboon, USA).

iridium layer for morphological analysis using a scanning electron microscope (SEM Teneo VS, FEI, USA) operated at 5 kV and a working distance of 66 and 10 mm.

Feed solutions were prepared using milli-Q water, NaCl (S271-1, Fisher Chemical, USA), Na_2SO_4 (223506, VWR, USA), $CaCl_2$ (223506, Sigma-Aldrich, USA), while pH was not regulated and varied between 6.9 and 7.4. For growth (G) experiments, an undersaturated solution was prepared by mixing equimolar proportions of calcium chloride and sodium sulfate from previously filtered (0.45 μm) stock solutions to a target concentration of 15 mM (total Ca^{2+} and SO_4^{2-}). For deposition (D) case, solid calcium chloride and sodium sulfate were added directly to Milli-Q water in equimolar proportions to create a highly supersaturated stock, which precipitated almost immediately upon mixing and was subsequently diluted to reach a suspension with total Ca^{2+} and SO_4^{2-} of 30 mM, comparable to the feed solution in G case after permeate abstraction at t = 0 (see Figure SM 3).

The experimental procedure aimed to distinguish between surface crystallization (G, for growth) and bulk crystallization (D, for deposition) in replicate runs (I/II). In the G(I–II) experiments, the membrane was compacted with a 30 mM NaCl solution and conditioned with an undersaturated $CaSO_4$ solution. Scaling was initiated by permeate abstraction until a feed concentration factor (CF) of 1.7 was reached, simulating supersaturation levels near the end of an RO pressure vessel under a recovery operation of 40 %. Subsequently, the system was operated in recirculation mode. A microfilter was installed in the concentrate line to remove any bulk-formed crystals. This approach was adapted from the methodologies described by Drak et al. [44] and Uchymiak et al. [28], enabled a controlled assessment of growth-driven scaling experiments.

In the D(I–II) experiments, a higher NaCl concentration (60 mM) was used during compaction and conditioning to approximate the ionic strength of the supersaturated feed solution achieved in the G(I–II) experiments. Scaling was induced by directly dosing a supersaturated $CaSO_4$ suspension into the feed, with the system operated in full recirculation mode. Unlike the growth-series experiments, no permeate abstraction was performed, and the microfilter was intentionally excluded to allow suspended crystals to remain in the system and deposit onto the membrane surface.

2.3. OCT imaging

Scaling development was monitored in real-time by two similar but not identical OCT systems (OCT-1: Scan rate 36 kHz, A-scan averaging 20; OCT-2: Scan rate 30 kHz, A-scan averaging 8; both Ganymede II, Thorlabs GmbH, Germany). OCT images were obtained at a fixed position in the central glass windows on the MFS, using the time series function every 8 min. The volumetric scans had a resolution of 10 × 10 × 2.2 μm (x,y,z), and a field of view of 499 × 499 × 558 voxels (x,y,z).

OCT image data were preprocessed using an in-house MATLAB (MathWorks, USA) script, where intensity values were normalized and smoothed [45,46]. By interpolation in x,y- and averaging in z-direction, a resolution of 8.8 × 8.8 × 8.8 μm was obtained and one spacer cell normalized to 3 × 3 mm was selected for further processing. Furthermore, image segmentation was performed by dividing pixels as above or below a threshold, defined as $T = \mu + 2\sigma$, where μ is the average signal and σ is the standard deviation, both determined by the MATLAB script.

Voxels where the signal exceeded the threshold ($S > T$) were considered a feature, while the rest were considered background. The initial image with an unfouled membrane was used as mask, to discriminate between membrane and spacer features vs fouling. Considering the needle-like geometry of gypsum crystals, the size of detected features would likely be affected by the smoothing procedure. Thus, to filter out noise, clusters of orthogonally connected voxels were determined by the MATLAB *bwconncomp* function, where clusters with less than 27 voxels (3D) or 16 pixels (2D) were considered noise.

Due to their needle-like geometry, large sections of crystals become visible at once, and due to translucency, they could partially disappear in later images. Voxels containing scaling ($S > T$) in > 95 % of the future images were marked, preventing these voxels from being filtered out, and to fill in these voxels for partial features being temporarily invisible. This procedure is illustrated in Fig. 2. We denote voxels as 'persistent fouling' if $S > T$ in > 95 % of the future images. We denote voxels as 'mobile fouling' if they meet all the requirements except that they are not considered a feature in > 95 % of the future images. Since the voxels denoted as mobile fouling are based only on the current scan, thus not benefiting from information from present or future scans, they are more susceptible to the artefacts sketched in Fig. 2.

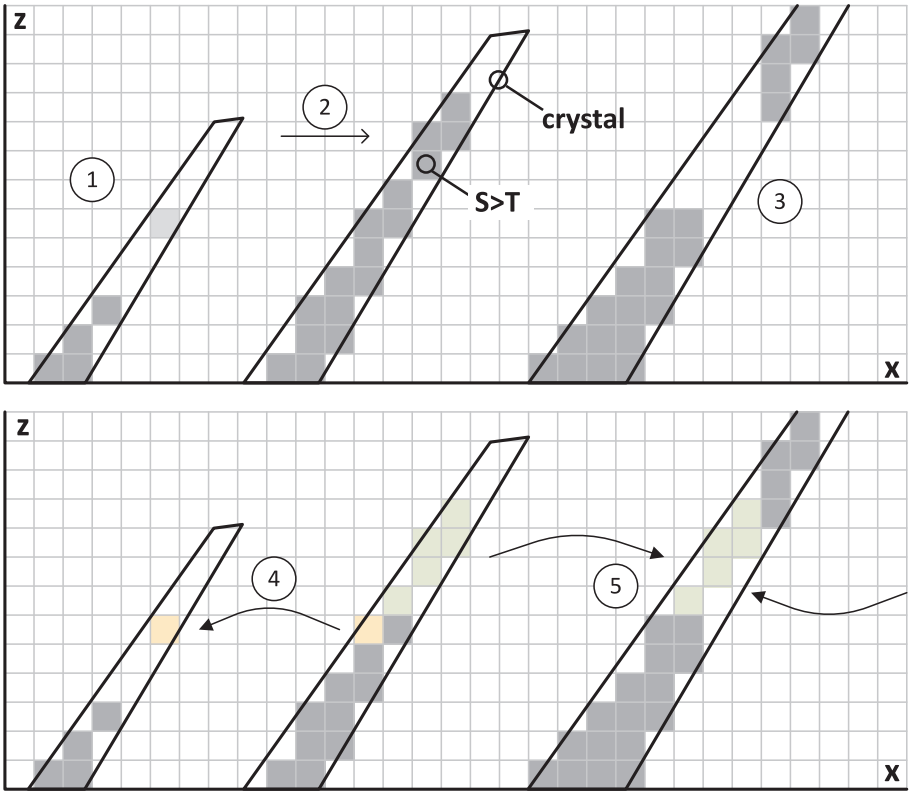

Fig. 2. Voxel classification and filtering approach for crystal detection. (1) Small, unconnected features (e.g., the light gray pixel) were typically filtered out. (2) Relatively long and thin features can suddenly appear, when signal exceeds the threshold ($S > T$). (3) Crystals may appear (partially) translucent (e.g., white pixels in the middle of a needle-like structure). (4) Voxels confirmed to be part of a crystal in future frames will not be filtered out (e.g., yellow pixel). (5) Voxels identified to be part of a crystal in both past and future frames were filled in to maintain continuity in detection.

Normally, a 2D slice is obtained by taking a one voxel-wide subset of the 3D volume data. The needle-like crystal geometry would lead to barely visible features, appearing sometimes as floating islands. To remedy this, slices were obtained by a N voxel-wide subset of the 3D data, where fouling is detected if $S > T$ in any of the N sub-slices. For example, a top view was obtained from merging maximum values from 15 *x,y*-layers above the membrane. The surface coverage was defined as the number of pixels with fouling divided by the total number of pixels on the surface. The fouling volume was calculated as the number of voxels with fouling multiplied by the voxel volume.

2.4. Water quality characterization

Water samples were collected from the concentrate (before the MF unit) and permeate streams during each experiment. Turbidity (2100Q, Hach, USA) and pH (Sentix 940, WTW, Germany) were measured immediately after sampling. Additional dilutions were prepared for cation (Na^+, Ca^{2+}) analysis using ICP-OES, and anion (Cl^-, SO_4^{2-}) analysis was conducted by ion chromatography (Dionex ICS-6000 DC, Thermo Scientific, USA).

Salt passage is defined as the permeate concentration ($c_{i,P}$) divided by feed concentration ($c_{i,F}$), $pas_i = \frac{c_{i,P}}{c_{i,F}}$. When concentrations are based on ICP-OES, the samples of feed and permeate are taken at the same time.

In addition to ICP-OES, the salt passage was continuously monitored by estimating NaCl concentration in the permeate from conductivity measurements, using a predetermined calibration curve that assumed the absence of Ca^{2+} and SO_4^{2-}. The feed NaCl concentration was determined using the initial Na^+ concentration in the feed (measured by ICP-OES) and corrected with the concentration factor, calculated based on real-time permeate flow and recovery monitoring.

2.5. Saturation index

The degree of supersaturation of soluble salts in aqueous solution is frequently expressed by the saturation index (*SI*) given by the logarithm of the ratio between the ion activity product and the solubility product of the salt, **(1)**:

$$SI = \log_{10}\left(\frac{a_{Ca}a_{SO4}}{K_{SP}}\right) \quad (1)$$

a_{Ca} and a_{SO4} are the activities of salt ions in solution and K_{sp} is the activity solubility product of the salt. A solution is unsaturated at $SI < 0$, saturated at $SI = 0$, and supersaturated at $SI > 0$.

The activity (a_i) is the product of the concentration (c_i) and activity coefficient (γ_i), $a_i = \gamma_i c_i$. The semi-empirical activity model of Davies [47] was used to express the γ_i as a function of ionic strength (I) for $I \leq 0.5$ M as shown in **(2)**:

$$\log_{10}(\gamma_i) = -Az_i^2\left(\frac{\sqrt{I}}{1+\sqrt{I}} - 0.3I\right) \quad (2)$$

where z_i is the charge of ion i, and the temperature-dependent coefficient A has a value of 0.509 at 25 °C when $I = \frac{1}{2}\sum c_i z_i^2$ is in mol/L. The free hydrochemistry software Aqion [48] was used to calculate the saturation index from measured ion concentrations, utilizing the thermodynamic database wateq4f.dat. The calculated values of SI are presented in Figure SM 1(a).

2.6. Computational fluid dynamics with solute transport and speciation

Computational Fluid Dynamics (CFD) was coupled with the transport (diffusion/ convection) and speciation equilibria of several ions/

molecules (Na^+, Cl^-, Ca^{2+}, SO_4^{2-}, $NaSO_4^-$ and $CaSO_4$), to evaluate the gypsum precipitation potential through the Saturation Index (SI). The numerical procedure and 3D computational domain were based on Cespedes et al. [49]. For this case, a mesh of 37×10^6 cells was used. The mesh independency was evaluated through the CP modulus on different meshes, considering different sizes of the first layer close to the membrane (30 μm − 5 μm) and the number of refinement layers (2 – 12). The model was solved using the commercial CFD software ANSYS Fluent 2023R2. For this study, a spacer-filled channel was used (dimensions of 42.5 × 4.24 × 0.71 mm, i.e. 10 spacer units). To prevent reversed outflow and inflow effects, additional spacer-less channel sections were included (Fig. 3). A description of model equations, numerical procedure, boundary conditions and parameters is presented in the Supplementary Material, Table SM 1 and Table SM 2.

To account for the development of the hydrodynamic and mass transfer boundary layers, the 8th spacer unit was selected for comparison with experimental results. Water quality data from the crystal growth experiments, measured after permeate abstraction to achieve supersaturation, were used as inlet concentrations for the model simulation.

3. Results and discussion

3.1. Impact of gypsum fouling on operational parameters

We conducted replicate experiments for conditions promoting predominantly deposition (DI and DII) versus predominantly growth (GI and GII) of gypsum crystals on the membrane. The growth experiment was started with an undersaturated solution, which was concentrated to a target SI by withdrawing permeate and reaching the target SI at $t = 0$, after which permeate and concentrate were both recycled to maintain a constant composition. In the deposition case, a suspension of preformed crystals was used as feed. The ions in solution were assumed to be in equilibrium (SI = 0). The total (dissolved plus precipitated) calcium sulfate in the suspension was chosen to be similar to the GI and GII solutions when a concentration factor of 1.7 was reached.

Fig. 4 shows the change of the major operational membrane performance indicators in time, namely: transmembrane pressure TMP (**a**), feed channel pressure drop ΔP (**b**), and solute passage *pas%* (**c**, **d**). Additional measurements of process parameters in time are shown in Figure SM 1 (feed water turbidity, pH and calculated SI), Figure SM 2 (feed water conductivity EC_F and temperature T, and permeate flux J_W), and Figure SM 3 (ion concentrations in feed $c_{Na,F}$, $c_{Cl,F}$, $c_{Ca,F}$, $c_{SO4,F}$).

Notably, the transmembrane pressure TMP exhibits a sharp increase to the maximum value, where the experiment had to be stopped (Fig. 4**a**). Up to the point at which scaling begins, constant TMP operation is functionally equivalent to constant flux operation, as both pressure and flux remain stable. However, once a substantial amount of scaling develops, constant TMP operation results in a decline in flux, whereas constant flux operation leads to an increase in TMP. In our experiments, the TMP increase started instantly in the deposition case (D) as the suspension already contained particulate matter. In the scaling growth case (G), the TMP increase started only after 3–4 days then raising sharply after 1–2 days. Induction time is defined as the delay between reaching supersaturation and the first detectable signs of crystal growth [50]. If operational performance is used as a fouling indicator, as is conventionally done in practice [51,52], our results suggest that there may be an induction time of ca 3–4 days when using TMP increase as an inorganic fouling indicator.

In practice, the feed channel pressure drop (ΔP) increase is commonly used as a fouling indicator and as a criterion for initiating chemical cleanings [14,42,53]. Fig. 4**b** shows the pressure drop monitored for each experiment. While the increase in DP looks steep (DII), the magnitude is moderate at ~ 20 to 40 mbar. The increase in pressure drop was less pronounced than the considerable rise in transmembrane pressure (TMP). Since an increase in pressure drop is typically indicative of fouling involving the feed spacer, this suggests that scaling occurred primarily on the membrane surface rather than on the feed spacer.

The measured salt passage is shown in Fig. 4, for the growth (**c**) and the deposition (**d**) cases. The NaCl passage estimated from permeate conductivity (lines) is in agreement with the passage determined from ion concentrations measured by ICP-OES (markers). Interestingly, the NaCl passage in the growth case (Fig. 4**c**) decreases as scaling occurs, while it is usually expected that fouling negatively impacts salt rejection. We hypothesize that the scaling growth blocks a part of the membrane, while increasing the local flux elsewhere because the setup was operated at constant permeate flux [54]. According to the solution diffusion (SD) model, the salt passage should decrease with increasing water flux J_W, provided that the increase in concentration polarization is not too strong, see **eqn. (3)** with salt permeability B, and mass transfer coefficient k:

$$pas = \frac{B\exp\left(\frac{J_W}{k}\right)}{B\exp\left(\frac{J_W}{k}\right) + J_W} \tag{3}$$

In contrast to Na^+ and Cl^-, we observe an almost constant passage for Ca^{2+} and SO_4^{2-}, which can be attributed to their lower diffusion coefficients (and therefore lower mass transfer coefficient k) and a less favorable net effect of increasing flux. While fouling may affect the

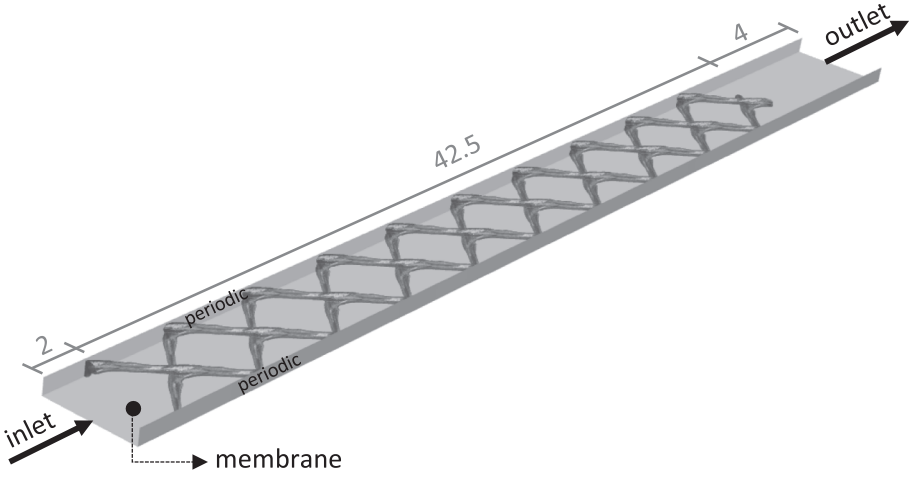

Fig. 3. Geometry used for the numerical model. The flow and mass transport with reactions were computed within a channel made by parallel plates separated by the spacer (10 units long), plus inlet/outlet zones (dimensions in mm).

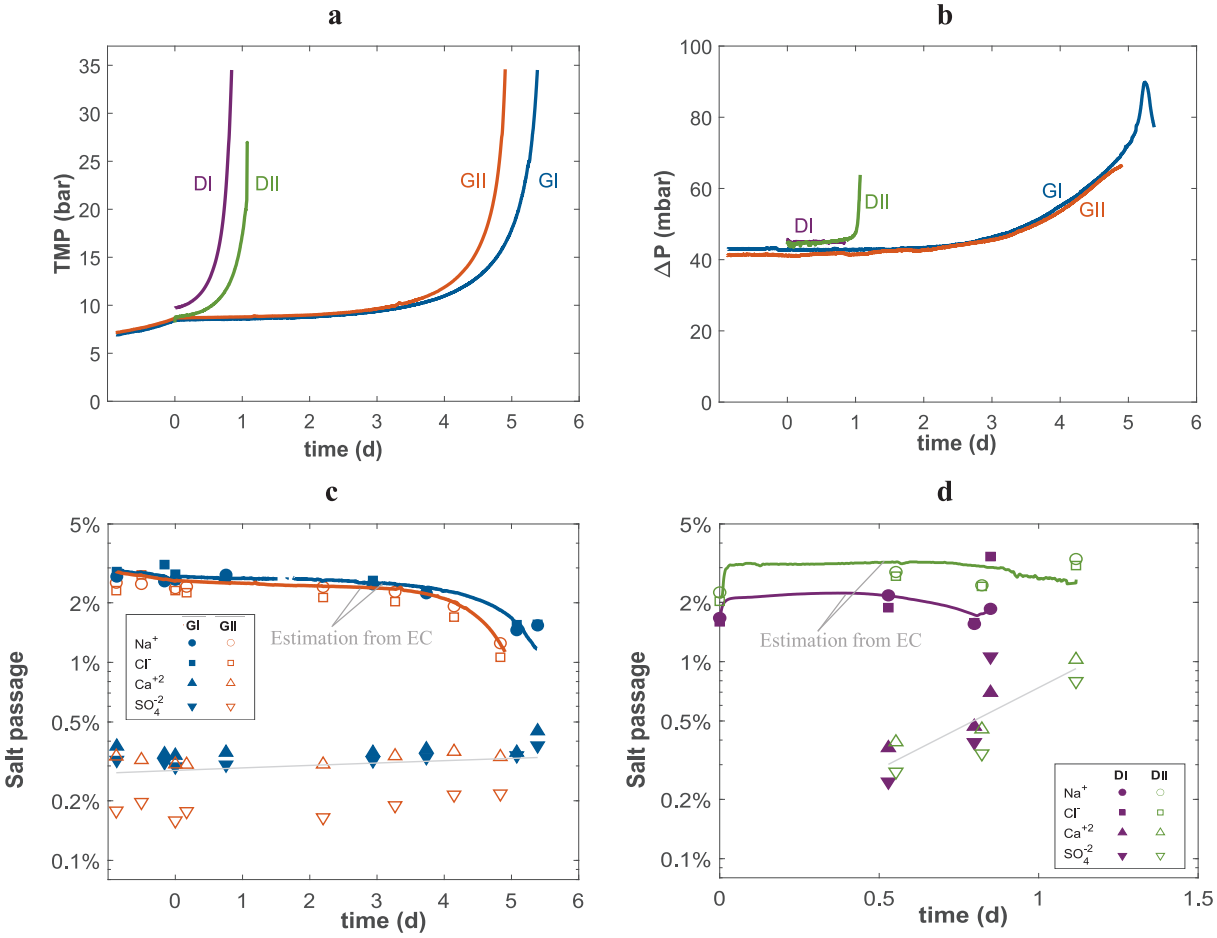

Fig. 4. Major operational parameters measured over time (days): **(a)** transmembrane pressure (TMP), **(b)** pressure drop (ΔP), **(c-d)** salt ions passage (pas%, on a log scale). Scaling experiments were conducted in two replicates for each growth (GI-II) and deposition (DI-II) cases. The estimated NaCl salt passage (solid lines) agrees well with the measured salt passage for Na^+ and Cl^- ions. Experiment DII ended at TMP 25 bar due to a controller error after 1.2 days affecting the flux regulation. Gray lines in the passage of Ca^{2+} and SO_4^{2-} are only included to guide the eye.

membrane surface charge, we consider that the internal membrane charge density regulating salt rejection [55,56] remains mainly unaffected. Moreover, any reduction in charge density due to Ca^{2+} interactions with negatively charged functional groups would increase the salt passage.

In the deposition case (Fig. 4**d**) the Na^+ and Cl^- (or NaCl) passage is roughly constant, while the passage of Ca^{2+} and SO_4^{2-} increases. The result is more in line with cake-enhanced concentration polarization [57]. Thus, based on the observed salt passage trends for divalent ions (Ca^{2+} and SO_4^{2-}), we tentatively infer that crystal growth results in localized membrane blockage, as indicated by minimal ions passage, whereas deposition appears to lead to the formation of a more porous and permeable fouling layer, reflected by increasing divalent ions passage.

3.2. *Optical coherence tomography for qualitative scaling progression analysis*

Along with real-time monitoring of operational parameters, we used OCT for acquiring *in-situ* time series of images (1 scan per 8 min) of the feed channel at a fixed position. The scanned location corresponded to the center of the membrane sheet, approximately 2 cm from the feed channel edge and 10 cm from the inlet, representing the midpoint in both width and length. Raw images were smoothed and processed to distinguish fouling (scale volume) from the feed channel components.

Fig. 5 presents the progression and spatial distribution of scaling measured from OCT imaging for both **(a)** growth (G) and **(b)** deposition (D) cases. The figure shows a top view (on the left) of membrane surface coverage and two side views (I, II), all representing the chosen one spacer unit. While typically OCT images are represented as a slice of width 1 pixel, we found that due to the aspect ratio of the needle-like crystals, this resulted in their poor visibility. For visualization, we combined several slices (15 pixels for the top view z and 40 for the side). The feed spacer and membrane from the initial OCT image (unfouled channel) were used as a mask depicted in gray, and the water-occupied space is light blue in this visualization. Mobile fouling (dark blue) was present at the time of the image, but not in > 95 % of later images, whereas the persistent fouling (white) was present permanently (>95 %) after the image was acquired. The area coverage with foulant is expressed as a percentage, shown next to the top view. Each image represents the first frame in which the area coverage (A_{cov}) reaches or exceeds the specified threshold (e.g., $A_{cov} \geq 5$ %).

In the growth case (Fig. 5**a**) initial scaling is on the top-left edge, adjacent to the feed spacer. It appears that most of the scaling is growing towards the center from a single small area. Comparing consecutive images, we can recognize the same feature in different images, increasing in size. Indeed, in these conditions, crystal growth occurred rather than particle deposition. When scaling progresses further (e.g.,>10 % coverage), it is apparent that crystals also grow from the bottom right edge spacer fiber. It is possible that those later crystals are expanding from the top left edge of the adjacent spacer cell, thus originating from the same area but shifted one spacer cell down-right. As the

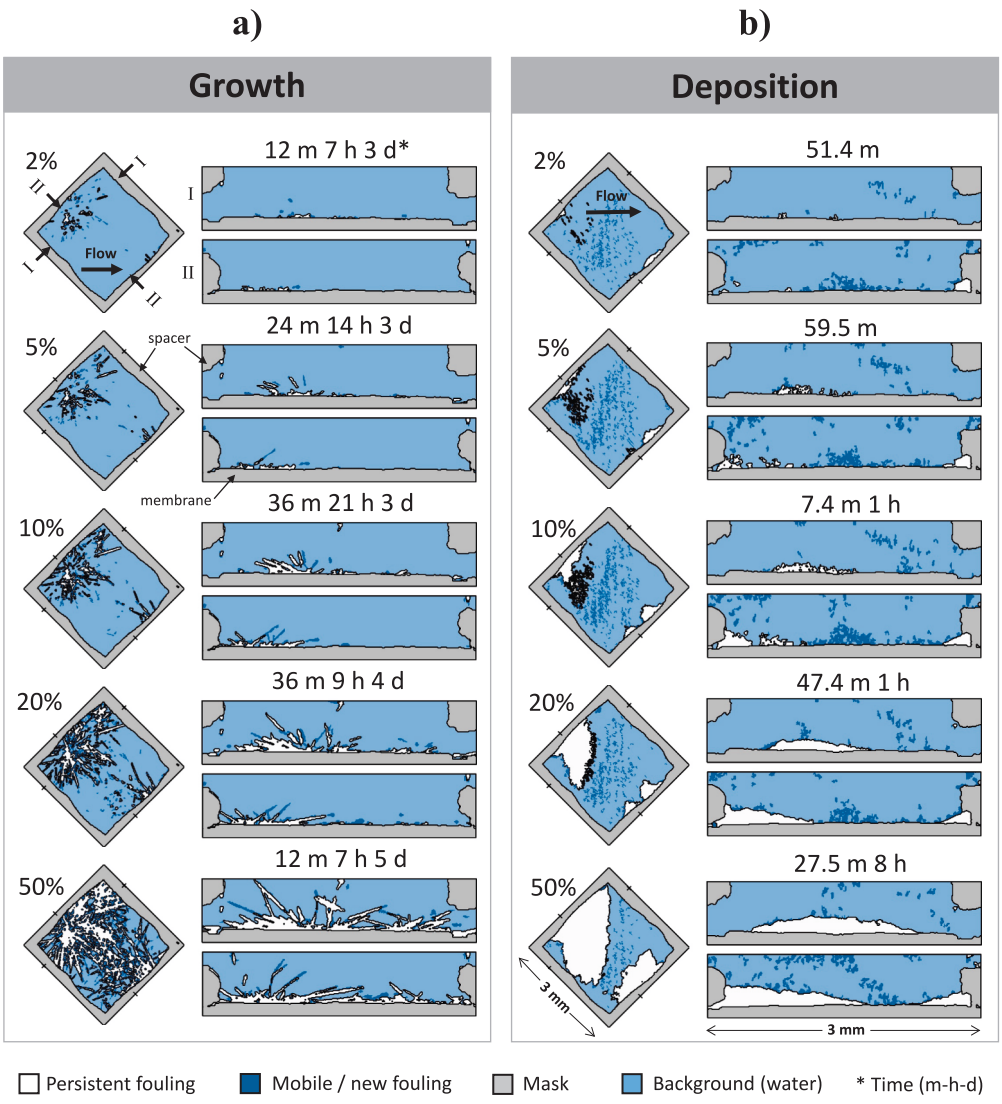

Fig. 5. Scaling progression and spatial distribution in the feed channel from OCT imaging for **(a)** growth (G) and **(b)** deposition (D) cases. OCT scans were performed at the center of the membrane sheet, approximately 2 cm from the edge and 10 cm from the inlet. Each image shows the first frame in which the area coverage (A_{cov}) reaches or exceeds the specified threshold ($A_{cov} \geq 2$ %, 5 %, 10 %, 20 %, and 50 %), with the corresponding time indicated on each image. Crystals are outlined in black to enhance visibility. Left: top-view images show the extent of surface coverage on the membrane delimited by the feed spacer (gray mask). Right: Cross-sectional views (I and II) illustrate the vertical distribution of scaling relative to the feed spacer and membrane (gray mask). Each scaling case exhibits distinct formation patterns: spike-like crystalline structures are observed for growth **(a)**, while the deposited layer **(b)** appears more uniform.

crystals grow and increase the area coverage, the needle-like crystalline structures characteristic of gypsum become more pronounced. The new/mobile fouling (dark blue) suggests that needles suddenly appear and will later disappear. We attribute this to the large aspect ratio of the crystals, where relatively large features may go undetected because their width does not span enough pixels – then a slight increase in thickness results in the entire feature appearing. Secondly, the crystals can be translucent and thus may be partially invisible (see Fig. 2). In addition, cross-sectional views (I-II) further confirmed that scaling did not develop around the feed spacer and did not occupy a large part of the flow channel, which is consistent with a moderate effect of the fouling on pressure drop (ΔP) (Fig. 4**b** GI and GII).

On the other hand, the top-view of the deposition case in Fig. 5**b** showed initial fouling slightly more dispersed, with a higher amount of new/mobile fouling (dark blue) compared to the growth case. This can be attributed to the presence of dispersed crystals, as indicated by the high turbidity of the feed suspension (> 900 NTU, see Figure SM 1). Cross-sectional views (I-II) revealed that scaling deposited on the membrane, without obstructing the flow over the top filament (I) or under the bottom filament (II). This could explain why we observed only a moderate pressure drop increase (Fig. 4**b** DI and DII). Unlike the distinct crystalline needles observed in the growth case, the deposited layer appears more uniform, resembling a typical cake layer. Large particles suspended in the water could be observed as the dark blue regions. Some porous structures of the cake layer can be recognized in the panels corresponding to 5 % and 10 % area coverage. Generally, the fouling appears solid, likely due to the resolution of the OCT being too course to detect the voids in the fouling layer.

3.3. *Quantification and characterization of fouling progression*

The application of imaging smoothing and processing techniques enabled a clear visualization and qualitative assessment of the scaling progression patterns in both the growth (G) and deposition (D) cases. In addition, OCT can provide data for the quantification of the degree of scaling in the feed channel, for example, the foulant volume and the area coverage. It is important to realize that when quantifying fouling from gray-scale images acquired by OCT, the results will depend on several

factors, such as the chosen threshold in segmentation and how noise was filtered out.

Fig. 6**a** shows the calculated fouling volume normalized per membrane area over time for each experiment. In the deposition scenario (DI and DII), we observed fouling right from the beginning because the suspension already contained visible crystals, whereas in the growth case (GI and GII), fouling commenced after 2–3 days. This suggests that an induction time of 2–3 days could be obtained from OCT imaging, in contrast to the 3–4 days inferred from operational parameters such as the sudden increase in TMP (Fig. 4**a**). This demonstrates that real-time, *in-situ* OCT imaging can detect scaling earlier than by monitoring operational parameters.

We also evaluated the number of crystals on the membrane surface (N_c) presented in Fig. 6**b** over time, based on the scaling area coverage illustrated in Fig. 5**a**. Here we defined a 'crystal' as a feature of at least 16 orthogonally connected pixels. Notably, the first crystal ($N_c = 1$) was detected by OCT within 1–2 days. This demonstrates that detecting individual crystals on the surface can be a more sensitive indicator of early crystal formation.

The impact of foulant relative volume on the required transmembrane pressure (TMP) is illustrated in Fig. 6**c**. In the growth case, the TMP sharply increased as fouling volume reached ca 30 $\mu m^3/\mu m^2$, whereas in the deposition case, TMP remained relatively stable, tolerating higher levels of fouling volume (80 – 90 $\mu m^3/\mu m^2$). This clearly shows that grown crystals affect the transmembrane pressure more strongly than deposited crystals, which can be attributed to the different structures of the scaling layers (e.g., porosities).

To further investigate the possible difference in structure, we measured the amount of calcium (Ca^{2+}) on the membrane through an autopsy. A fouled membrane coupon of ca. 3 × 4 cm was cut from the visually inspected membrane area, corresponding to the OCT observation window, and then suspended in an acid solution (HNO_3 1 %) to dissolve the scaling, followed by cation analysis via ICP-OES. Fig. 6**d** presents the obtained mass of gypsum per area. The results show that the accumulated gypsum per membrane area was similar for both growth and deposition cases, with values around 50 g gypsum/m^2. We note that some of the fouling layer may have been disturbed when lifting the membrane sheet from the MFS and during the process of cutting the coupons for immersion in the acid solution. Thus, the amount of scaling determined in the autopsy is likely underestimated.

Using the measured foulant mass (Fig. 6**d**) and assuming it consists of gypsum ($CaSO_4{\cdot}2H_2O$) with density 2.3 g/mL [58], we calculated the volume of gypsum per membrane area from the autopsy (V_A). We assumed that the final volume per area (V_{OCT}), as shown in Fig. 6**a**, represents the volume consisting of crystals and voids just before the autopsy. The porosity ϕ of the fouling layer can now be estimated by $\phi = 1 - V_A/V_{OCT}$. The results (Fig. 6**e**) indicate that the fouling layer porosity for the deposition (80 % voids) is notably higher than that obtained by crystal growth (40–60 % voids or water), confirming the suspected structural differences resulting from the deposition and growth cases.

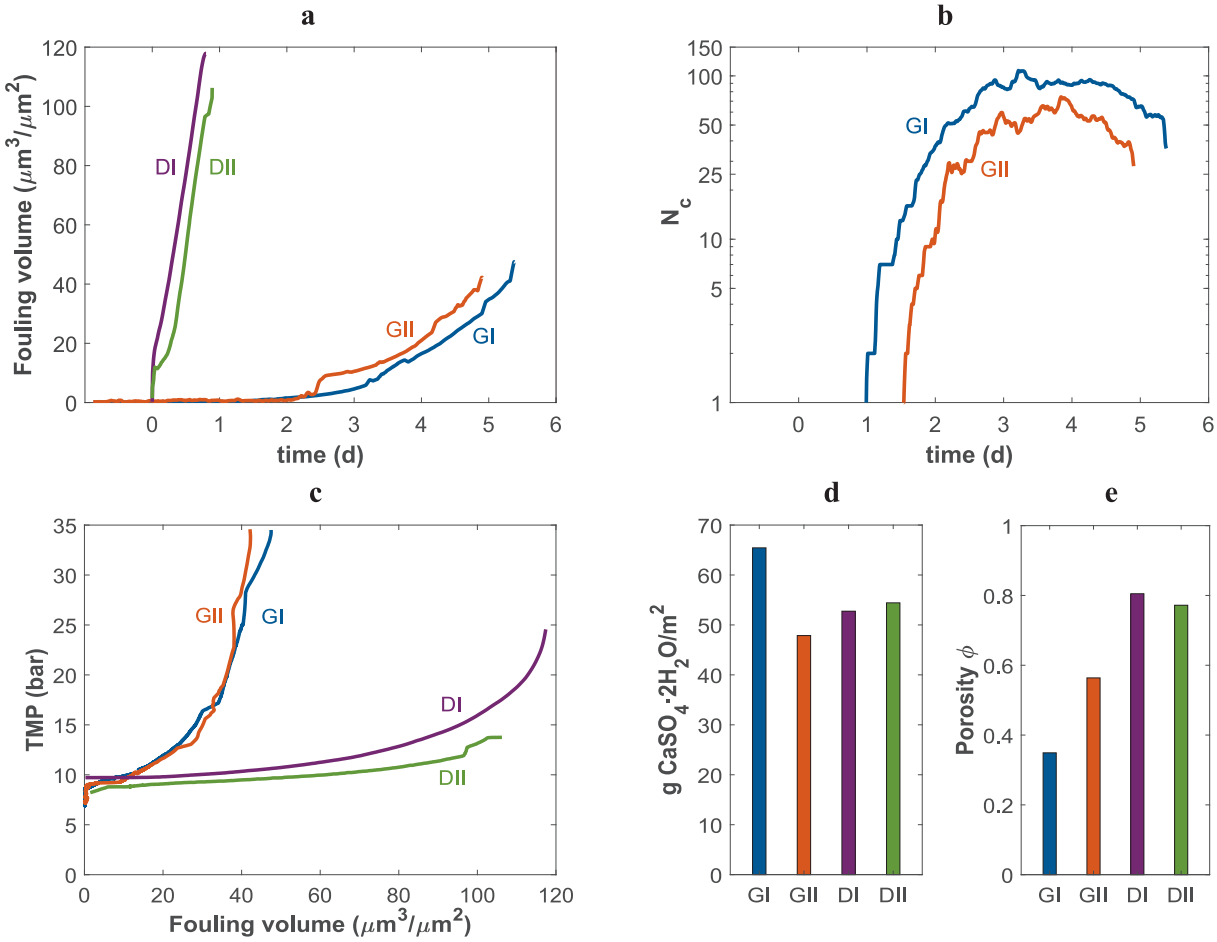

Fig. 6. (**a**) Foulant volume per membrane area over time, suggesting an induction time of ca. 2 days for the growth case (G) and immediate deposition (D cases). (**b**) Number of crystals in one spacer unit (N_c, log scale) over time, showing the first crystals in the growth cases (GI and GII) within 1–2 days. (**c**) Transmembrane pressure (TMP) function of relative fouling volume, showing the stronger impact of growth (G) than of deposition (D). (**d**) Gypsum mass per membrane area measured from autopsy. (**e**) Calculated porosity of the fouling layer, with higher porosity observed in the deposition cases compared to the growth cases. The values presented in (d) and (e) correspond to the final time point of the operational monitoring shown in Fig. 4**a,b** and the final time points in (**a**).

One might expect a randomly stacked fouling layer to have a porosity of about 40 % however, the porosity of the fouling layer was higher than expected, this could be explained by underestimating the amount of fouling in the autopsy and/or overestimating the amount of fouling in OCT.

To investigate the morphology of the fouling layer formed under growth and deposition conditions, membrane samples taken from the autopsy were also analyzed using optical and SEM imaging. Pristine membrane samples were also examined as a reference.

Optical imaging revealed that in the growth case, no significant differences were observed along the membrane length, as indicated by similar scaling patterns in membrane coupons collected near the inlet and outlet regions (Figure SM 4a,b). However, a clear contrast was identified along the width, between the membrane center and edges, with a larger concentration of crystals near the edges and even within the gap next to the O-ring (Figure SM 4c,d). Notably, growth patterns were consistent across different spacer cells. These observations suggest that, apart from localized edge effects, the overall fouling distribution was relatively homogeneous across the membrane surface. Optical images supporting these observations are provided in Figure SM 4 and Figure SM 5.

This spatial distribution contrasts with findings reported by Rahardianto et al. [59], who observed a clear gradient in gypsum scale coverage along the membrane length, particularly toward the outlet region. Their study was conducted without spacers, which likely resulted in stronger axial gradients of concentration polarization. In our study, the use of a feed spacer contributes to more uniform flow distribution and reduced axial concentration polarization, which may explain

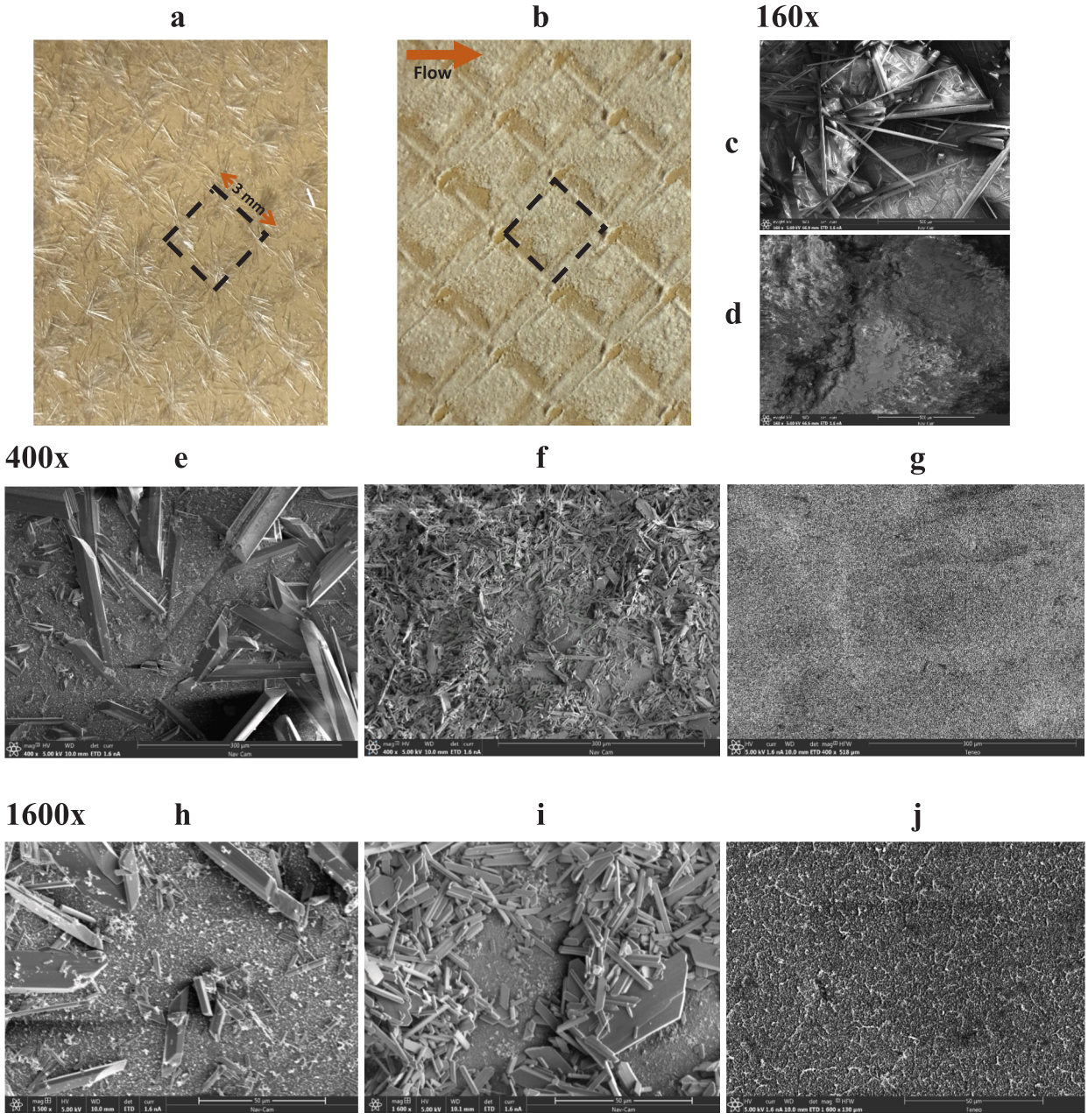

Fig. 7. Optical and SEM images of the fouled surfaces. Optical images of the grown (**a**) and deposited crystals (**b**), with dashed boxes indicating the previous location of the feed spacer. SEM images for growth (**c**) and deposition (**d**) at 160 × magnification; growth (**e**), deposition (**f**) and pristine membrane (**g**) at 400×; growth (**h**), deposition (**i**) and pristine membrane (**j**) at 1600 × . A clear difference in aspect ratios was observed between the two cases, with significantly larger crystals forming in the growth case.

the relatively uniform fouling pattern along the length. Additionally, the relatively short length of our flow cell may not fully capture the axial scaling effects that are typically observed in full-scale modules, where scaling commonly occurs near the end of the last membrane element. Finally, it is important to note that autopsy imaging only provides a final snapshot of the fouling distribution and does not reveal the precise location or timing of the initial scale formation.

Close up optical images for the fouled membrane for growth and deposition cases are shown in Fig. 7**a,b** with marked previous location of the feed spacer. In the growth (G) case crystals were sharp, needle-like and translucent (Fig. 7**a**), while the deposition (D) case showed a more amorphous, white fouling layer (Fig. 7**b**). These visual morphological differences align well with the OCT top-view observations identified in Fig. 5.

SEM imaging provided further insight into the crystal morphology. At a low magnification of 160×, needle-like crystals were already visible in the growth case (Fig. 7**c**), whereas the deposition case (Fig. 7**d**) showed a fouling layer without distinct crystal shapes or sizes. While the images predominantly showed large needle-like structures, some smaller rhombic crystals were also visible, suggesting that deposition of bulk crystals may have occurred also. Possibly, these differences are caused by different degrees in super saturation during their formation. However, Shih et al. [60], similarly distinguished between surface and bulk crystallization by examining membrane gypsum scaling with and without retentate filtration. In their study, filtration of the retentate promoted the formation of well-defined rosette structures composed of gypsum needles, indicative of surface crystallization, while unfiltered conditions led to the deposition of fractured and irregular bulk-formed crystals on the membrane surface. Our comparison further supports the interpretation that the growth-case in our experiments is dominated by surface crystallization, while the deposition case results in a more amorphous layer likely formed by the accumulation of bulk crystals.

Fig. 7**e,f** show SEM images at 400 × magnification for the growth and deposition cases, at selected spots that included regions with exposed membrane, allowing direct comparison with the pristine membrane surface in Fig. 7**g**. Crystals with typical dimensions of 25 by 170–500 μm were identifiable for growth (Fig. 7**c,e**). In contrast, for deposition individual crystals were hardly distinguishable (Fig. 7**f**), but rather an accumulation of smaller particles was observed. At an increased magnification of 1600×, rhombohedral crystals with typical dimensions of 3 × 10 μm were identified (Fig. 7**h**). In the deposition case, although the fouling layer appeared dense at low magnification, higher magnification images in Fig. 7**f,i** showed voids exposing bare membrane. The feed suspension used for deposition was circulated continuously. Possibly the crystals could be damaged by the feed pump. However, the crystals in the deposition case had sharp edges and did not appear abraded. Additional SEM images at various magnifications, along with crystal measurements for both growth and deposition cases, are presented in Figure SM 6.

3.4. Influence of supersaturation and concentration polarization on early-stage scaling

By using the time-series of OCT data, we identified the locations of initial crystal formation and counted the number of crystals formed over time (Fig. 6**b**). To further investigate the factors inducing crystal formation in early-stage scaling, we coupled developed computational fluid dynamics with multicomponent solute mass transport and speciation reactions. Simulations were set to compute the local distributions of solute concentration polarization (CP) and gypsum saturation index (SI), and possible correlate these with places of early nucleation and crystal growth.

The computed SI distribution on the membrane within one spacer unit (#8 on the model length) was plotted in Fig. 8 as a colored surface, with superposed OCT-derived crystal coverage (black/white contours) for both growth experiments. The first five crystals detected closely corresponded to the areas of highest SI, thus also of largest CP. This strong spatial correlation suggests that localized supersaturation plays the expected key role in determining where the first crystals appear.

According to the classical nucleation theory, the nucleation rate R_N (i.e., the number of new nuclei formed per area per time unit) is expressed as a function of local supersaturation ratio ($S = \frac{a_{Ca}a_{SO4}}{K_{SP}}$) in solution or solubility index (SI) [50]:

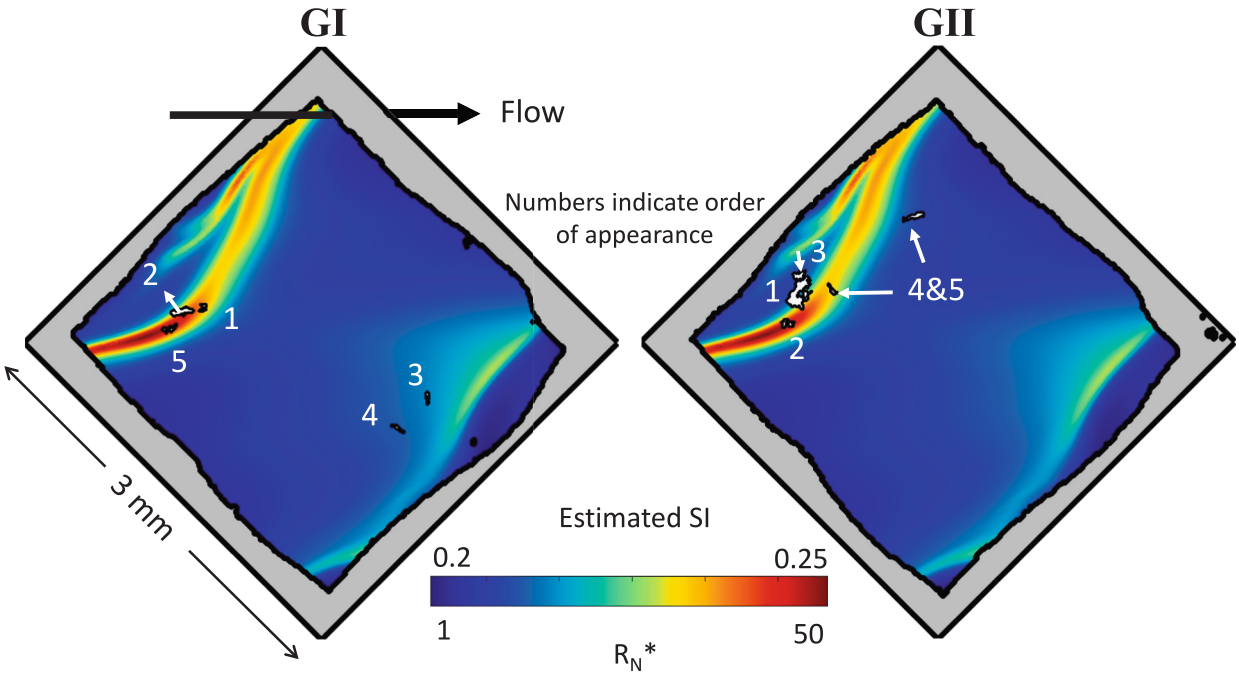

Fig. 8. Superposition of OCT-derived area coverage (black/white contours) with CFD/mass transport-simulated saturation index (SI) and relative nucleation rate (R_N*)(normalized with R_N*=1 at SI 0.2) for growth cases GI (left) and GII (right). The five numbered clusters mark the first detected scaling regions, which strongly correlate with areas of maximum SI and R_N thus suggesting that localized supersaturation is key in determining the initial crystallization sites.

$$R_N = A_N \exp\left(-\frac{a_N}{(\ln S)^2}\right) = A_N \exp\left(-\frac{a'_N}{SI^2}\right) \quad (4)$$

where A_N is a pre-exponential rate parameter and a_N or a'_N depend on the crystal type (molar volume), interfacial tension between the membrane and nucleus, and temperature. This strong non-linearity implies that even a small error in predicting the degree of saturation (SI) could lead to large deviations in the estimated nucleation rate, thus R_N predictions based on SI can be unreliable. Theoretical calculations with S and **eqn. (4)** with parameters from Lyster et al. [30] (A_N = 175 $cm^{-2}h^{-1}$, a_N = 2.36) predicted a maximum nucleation rate of ~ 0.4 nuclei/m^2/s, whereas our experimental observations indicate a significantly higher rate, reinforcing the limitations of classical S-based predictions. Instead, we can represent a nucleation rate normalized (R_N*) to the minimum nucleation rate obtained at SI = 0.2 (i.e., S = 1.585). In this case, the maximum rate obtained at SI = 0.25 (i.e., S = 1.778, see Figure SM 7) appears to be more than 50 times faster than the minimum (Fig. 8). This reinforces the idea that apparently small differences in SI caused by specific fluid dynamics interaction with solute mass transport (see Figure SM 8 and Figure SM 9) can cause large differences in the relative nucleation rate over the membrane surface.

It appears from OCT that almost all crystals originate from the same area that was identified in Fig. 8. While the entire membrane area was supersaturated, only the areas with the highest CP formed crystals (see Figure SM 8). Furthermore, crystal growth requires lower supersaturation than does the nucleation, allowing crystals to expand into areas with relatively lower supersaturation. Interestingly, as scaling accumulates in the highest CP regions, it may alter local transport conditions, slightly reducing overall CP and redistributing concentration gradients across the membrane surface.

The observed scaling patterns were reproducible across experiments, consistently forming at the same location within each spacer unit. Although the variations in saturation index (SI) across the membrane were relatively small, scaling did not occur randomly but instead originated at specific points. If the relative nucleation rate was less sensitive for SI, scaling would be expected to develop more uniformly across the spacer cell. However, its consistent localization suggests a highly nonlinear dependence on SI, where even small differences in supersaturation (~0.2–0.25) lead to significant differences in relative nucleation rate (~1–50). This indicates that certain regions within the spacer cell experience conditions that strongly favor initial crystal formation, reinforcing the idea that SI plays a dominant role in determining the onset and location of scaling.

3.5. Surface coverage vs cake layer

A comparison between growth- and deposition-driven scaling showed (i) salt passage decreased in the crystal growth case but increased in the deposition case, (ii) TMP increased significantly more per unit of fouling volume in the growth case, whereas deposition tolerated a higher fouling volume before causing significant TMP increases, and (iii) the estimated differences in foulant layer porosity further support the distinction between a more solid, surface-blocking structure and a more permeable, cake-like structure. This suggested that the *in- situ* grown crystals form solid structures that completely cover the membrane locally, blocking the passage, while leaving the rest of the area relatively unaffected. Gilron et al. [61] proposed this fouling mechanism, where scaling and resulting flux decline are primarily due to membrane surface blockage caused by lateral growth of crystals, rather than due to the hydraulic resistance of a growing cake layer. OCT imaging further supported this perspective, as we observed scaling through growth on the membrane surface in the experiments GI and GII, which contributed to surface blockage.

A key distinction between different studies lies in the experimental conditions. Constant pressure fouling experiments are more commonly reported in the literature [12,61,62], where scaling reduces the active membrane area, leading to an overall decline in flux. In contrast, the present study was conducted under constant flux conditions, requiring an increase in pressure to compensate for the loss of active membrane area. This adjustment resulted in intensified localized flux in the remaining active regions. As a result, the effect of scaling may be more pronounced in constant flux experiments compared to constant pressure experiments, where the flux decline is more evenly distributed across the membrane surface. This observation aligns with the findings of Radu et al. [54], who reported using a 2D mechanistic model for scaling, that operational mode influences scale formation, with greater precipitation occurring under constant flux compared to constant pressure operation.

3.6. Growth vs deposition

While we aimed to compare growth and deposition, we cannot fully exclude growth from occurring in the deposition case, nor deposition of bulk crystals in the growth case. Nevertheless, we believe that growth dominates in G and deposition dominates in D.

In the SEM images for case G (see Fig. 7**e,h**) needle-like crystals can be seen on top of other crystals, which may suggest those were deposited. We consider it more likely that due to sample handling, fragile structures were damaged. These crystals are much larger than 1 μm and would have been filtered out by the MF unit if they were in suspension. While 1 μm is likely insufficient to remove nano-sized precursors [63], we estimate with the residence of about 1–2 s (0.16 m/s and 20 cm length), crystals could not grow to a substantial size in one pass, therefore crystals (much) larger than 1 μm would have to develop on the membrane. This was confirmed by the OCT time series, where we could observe the needle-like crystals growing in time (see Fig. 5**a**). Secondly, no evidence of bulk crystallization was observed, as confirmed by the delayed TMP increase (Fig. 4**a),** the stable turbidity measurements below 0.3 NTU (see Figure SM 1c), and stable feedwater composition (constant SI), throughout the entire experiment (Figure SM 1a). Due to the recovery of only 1.25 %, we consider it unlikely that the turbidity changed in the flow channel, this is supported by the 1000 NTU turbidity found in the D experiment.

In the deposition case, we assume that the dissolved ions are in equilibrium with the bulk crystals (SI = 0). From the CFD results (Fig. 8), we estimate a maximum concentration polarization modulus of about 1.12, leading to a local SI of 0.05 at the membrane surface. Considering the strongly non-linear relation between SI and nucleation rate, we believe it unlikely that new crystals form on the membrane surface under those conditions. Likely, super saturation occurring near the membrane in the D case, would result of slight growth of already deposited crystals.

In light of previous studies (e.g., Mullin [50], Liu [64]), it is important to consider the possibility that gypsum nucleation may initiate heterogeneously on natural solid nanoimpurities, which are known to exist even in ultra-pure chemicals [65] in idealized conditions. In practice, however, it may be challenging to distinguish between nucleation occurring via nano-precursors formed in the liquid phase near the membrane surface and heterogeneous nucleation directly on the membrane material. Due to concentration polarization (CP) and the non-linear relationship with supersaturation, such precursors would likely form and deposit close to the membrane where local hydrodynamics would promote their deposition. Alternatively, heterogeneous nucleation may occur directly on the membrane material itself. More targeted studies would be needed to decouple these mechanisms and quantify their individual contributions.

3.7. Comparison of 'induction time'

Induction time (IT), defined as the interval between supersaturation and detectable crystal formation [50], is a key indicator for characterizing nucleation kinetics in membrane scaling. It plays a critical role in

understanding crystallization behavior and is widely used to design and optimize operational strategies for brine treatment, helping to assess and manage scaling risk [22].

For homogeneous nucleation, IT is commonly measured in batch reactors by monitoring changes in bulk solution properties. Indirect detection methods include measurements of electrical conductivity [66,67], pH [68], turbidity [69], and light transmittance [70]. Additionally, direct measurements of ion depletion can be performed using ion-selective electrodes (ISEs), particularly, calcium precipitation can be quantified by comparing Ca^{2+} concentrations before and after scaling occurs [67].

It is often assumed that no scaling occurs during the induction time, leading to the idea that scaling can be prevented if the feed water residence time is shorter than the IT [71]. Still, the residence time of water may not be relevant for crystals growth on the membrane, meaning that scaling can still occur over extended operational periods. Furthermore, IT is always defined relative to the detection method used: a more sensitive detection method results in a shorter measured IT. In our study, specifically for the growth case experiments (G), transmembrane pressure changes suggest an IT of 3–4 days (Fig. 4**a**), OCT-based volume analysis indicate 2–3 days (Fig. 6**a**), and direct crystal counting estimates are even shorter at 1–2 days (Fig. 6**b**). With an even more sensitive method, the IT would likely be even lower – also because the induction time is related to the apparition of the minimum-size stable crystal. While the concept of IT suggests a delay before visible scaling, nucleation may start immediately at $SI > 0$, and IT is merely determined by the smallest detectable crystals.

The concept of "induction time" for scale formation has been widely defined and applied in previous studies. Boerlage at al. [72] defined safe and unsafe operating limits for scaling in RO systems by calculating induction time based on supersaturation and temperature, correlating it with observed RO concentrate during various operating modes. Lyster et al. [30] implemented induction time, or 'growth retardation', based on direct visual observations on the membrane, to quantify the retardation of mineral crystal nucleation and growth in RO systems, assessing antiscalants effectiveness. Despite these advances, the true onset of membrane scaling remains unclear, as several studies that use various process parameter measurements often lead to conflicting interpretations of when scaling begins. For example, when computing the gypsum nucleation rate with parameters from [30], we obtained inferior rates to those we determined experimentally – even when working in the same range of saturation indices.

Common parameters employed to determine the onset of scaling, such as the measurable increase in bulk fluid turbidity, reduction in permeate flux (in constant pressure filtration), or changes in Ca^{2+} ion concentration and pH, lack sufficient sensitivity for accurately identifying the true onset of membrane scaling. While these criteria may be useful for general studies on scaling or precipitation, they are inadequate for precisely identifying when membrane scaling begins [33]. OCT, however, has the potential to serve as an early detection method for scaling, providing valuable insights into the initial stages of crystal formation before conventional monitoring techniques detect significant fouling.

4. Conclusions

A methodology was developed to promote scaling using an artificial solution under constant flux operation, enabling real-time monitoring and systematic analysis of scaling behavior. Transmembrane pressure increased more significantly than pressure drop, indicating that fouling predominantly occurred on the membrane surface. Salt passage trends further distinguished the mechanisms: NaCl passage decrease in growth-driven scaling suggested localized flux redistribution, while $CaSO_4$ passage increase in the deposition case indicated cake-enhanced concentration polarization.

Structural differences between the fouling layers were evidenced by OCT and SEM imaging. Growth-driven $CaSO_4$ scaling produced sharp, translucent crystals, whereas deposition resulted in an amorphous, white fouling layer. Quantitative OCT analysis enabled tracking of scaling progression, and membrane autopsy confirmed the higher porosity of the deposited layer.

The strong correlation between OCT-detected crystals and regions of high saturation index, simulated by CFD, demonstrated its potential as a spatially resolved early-warning tool. Differences in induction time across detection methods highlight the importance of sensitivity in scaling diagnostics and challenge the reliability of induction time as a scaling potential indicator.

Finally, the agreement between experimental and simulated data emphasizes the value of combining real-time measurement and modeling. OCT demonstrated potential as an early detection tool for scaling and could be further developed for inline monitoring in plant concentrate streams, enabling more precise control of operational conditions. This approach opens the door to chemical-free operation and provides a platform for systematic studies aimed at optimizing industrial-scale membrane processes.

CRediT authorship contribution statement

Natalia Franco-Clavijo: Writing – original draft, Methodology, Formal analysis, Data curation, Conceptualization. **Santiago Cespedes:** Writing – original draft, Formal analysis, Data curation. **Andreia Farinha:** Writing – review & editing, Supervision, Resources, Investigation, Formal analysis. **Geert-Jan Witkamp:** Writing – review & editing, Supervision, Methodology, Investigation, Funding acquisition, Conceptualization. **Cristian Picioreanu:** Writing – review & editing, Supervision, Resources, Investigation, Formal analysis, Conceptualization. **Johannes S. Vrouwenvelder:** Writing – review & editing, Supervision, Resources, Methodology, Investigation, Funding acquisition. **Bastiaan Blankert:** Writing – original draft, Visualization, Validation, Supervision, Methodology, Investigation, Formal analysis, Data curation, Conceptualization.

Declaration of competing interest

The authors declare that they have no known competing financial interests or personal relationships that could have appeared to influence the work reported in this paper.

Acknowledgments

The research reported in this paper was supported by funding from King Abdullah University of Science and Technology (KAUST), Saudi Arabia. The authors gratefully acknowledge the support of the Water Desalination Research Platform (WDRP) staff. Computational resources were provided by the Supercomputing Core Laboratory at KAUST, utilizing the Shaheen III system.

Appendix A. Supplementary data

Supplementary data to this article can be found online at https://doi.org/10.1016/j.seppur.2025.134664.

References

[1] M.A. Shannon, P.W. Bohn, M. Elimelech, J.G. Georgiadis, B.J. Mariñas, A. M. Mayes, Science and technology for water purification in the coming decades, Nature 452 (2008) 301–310.
[2] M. Elimelech, W.A. Phillip, The future of seawater desalination: energy, technology, and the environment, Science 333 (2011) 712–717.
[3] A. Panagopoulos, K.-J. Haralambous, M. Loizidou, Desalination brine disposal methods and treatment technologies-a review, Sci. Total Environ. 693 (2019) 133545.

[4] E. Jones, M. Qadir, M.T.H. van Vliet, V. Smakhtin, S.-M. Kang, The state of desalination and brine production: a global outlook, Sci. Total Environ. 657 (2019) 1343–1356.
[5] S. Lattemann, T. Höpner, Environmental impact and impact assessment of seawater desalination, Desalination 220 (2008) 1–15.
[6] S. Lattemann, M.D. Kennedy, G. Amy, Seawater desalination—a green technology? J Water Supply.: Res. Technol.—AQUA 59 (2010) 134–151.
[7] I. Ihsanullah, M.A. Atieh, M. Sajid, M.K. Nazal, Desalination and environment: a critical analysis of impacts, mitigation strategies, and greener desalination technologies, Sci. Total Environ. 780 (2021) 146585.
[8] T.M. Missimer, R.G. Maliva, Environmental issues in seawater reverse osmosis desalination: intakes and outfalls, Desalination 434 (2018) 198–215.
[9] G. Amy, N. Ghaffour, Z. Li, L. Francis, R.V. Linares, T. Missimer, S. Lattemann, Membrane-based seawater desalination: present and future prospects, Desalination 401 (2017) 16–21.
[10] J. Kucera, Reverse osmosis, John Wiley & Sons, 2023.
[11] A. Antony, J.H. Low, S. Gray, A.E. Childress, P. Le-Clech, G. Leslie, Scale formation and control in high pressure membrane water treatment systems: a review, J. Membr. Sci. 383 (2011) 1–16.
[12] M. Okazaki, S. Kimura, Scale formation on reverse osmosis membranes, in: Kagaku Kogaku Benran, (Chem. Engrg. Handbook), 1984, pp. 145-151.
[13] C.A.C. Van De Lisdonk, J.A.M. Van Paassen, J.C. Schippers, Monitoring scaling in nanofiltration and reverse osmosis membrane systems, Desalination 132 (2000) 101–108.
[14] Dupont, FilmTec™ Reverse Osmosis Membranes Technical Manual, Water solutions, (2023).
[15] O. Heinz, M. Aghajani, A.R. Greenberg, Y. Ding, Surface-patterning of polymeric membranes: fabrication and performance, Curr. Opin. Chem. Eng. 20 (2018) 1–12.
[16] A.G. Pervov, Precipitation of calcium carbonate in reverse osmosis retentate flow by means of seeded techniques — a tool to increase recovery, Desalination 368 (2015) 140–151.
[17] T. Tong, A.F. Wallace, S. Zhao, Z. Wang, Mineral scaling in membrane desalination: mechanisms, mitigation strategies, and feasibility of scaling-resistant membranes, J. Membr. Sci. 579 (2019) 52–69.
[18] H. Saleem, S.J. Zaidi, Nanoparticles in reverse osmosis membranes for desalination: a state of the art review, Desalination 475 (2020) 114171.
[19] A. Rahardianto, J. Gao, C.J. Gabelich, M.D. Williams, Y. Cohen, High recovery membrane desalting of low-salinity brackish water: Integration of accelerated precipitation softening with membrane RO, J. Membr. Sci. 289 (2007) 123–137.
[20] Q. Liu, G.-R. Xu, R. Das, Inorganic scaling in reverse osmosis (RO) desalination: mechanisms, monitoring, and inhibition strategies, Desalination 468 (2019) 114065.
[21] J.W. Gibbs, On the equilibrium of heterogeneous substances, Am. J. Sci. 3 (1878) 441–458.
[22] J. Rolf, T. Cao, X. Huang, C. Boo, Q. Li, M. Elimelech, Inorganic Scaling in Membrane Desalination: Models, Mechanisms, and Characterization Methods, in: Environmental Science and Technology, American Chemical Society, 2022, pp. 7484-7511.
[23] M. Gloede, T. Melin, Physical aspects of membrane scaling, Desalination 224 (2008) 71–75.
[24] S. Lee, J. Kim, C.-H. Lee, Analysis of CaSO4 scale formation mechanism in various nanofiltration modules, J. Membr. Sci. 163 (1999) 63–74.
[25] H.-J. Oh, Y.-K. Choung, S. Lee, J.-S. Choi, T.-M. Hwang, J.H. Kim, Scale formation in reverse osmosis desalination: model development, Desalination 238 (2009) 333–346.
[26] A.J. Karabelas, A. Karanasiou, S.T. Mitrouli, Incipient membrane scaling by calcium sulfate during desalination in narrow spacer-filled channels, Desalination 345 (2014) 146–157.
[27] M. Amin Saad, Early discovery of RO membrane fouling and real-time monitoring of plant performance for optimizing cost of water, Desalination 165 (2004) 183–191.
[28] M. Uchymiak, A.R. Bartman, N. Daltrophe, M. Weissman, J. Gilron, P. D. Christofides, W.J. Kaiser, Y. Cohen, Brackish water reverse osmosis BWRO) operation in feed flow reversal mode using an ex situ scale observation detector (EXSOD, J. Membr. Sci. 341 (2009) 60–66.
[29] M. Uchymiak, A. Rahardianto, E. Lyster, J. Glater, Y. Cohen, A novel RO ex situ scale observation detector (EXSOD) for mineral scale characterization and early detection, J. Membr. Sci. 291 (2007) 86–95.
[30] E. Lyster, M.-M. Kim, J. Au, Y. Cohen, A method for evaluating antiscalant retardation of crystal nucleation and growth on RO membranes, J. Membr. Sci. 364 (2010) 122–131.
[31] A.P. Mairal, A.R. Greenberg, W.B. Krantz, Investigation of membrane fouling and cleaning using ultrasonic time-domain reflectometry, Desalination 130 (2000) 45–60.
[32] Z. Hu, A. Antony, G. Leslie, P. Le-Clech, Real-time monitoring of scale formation in reverse osmosis using electrical impedance spectroscopy, J. Membr. Sci. 453 (2014) 320–327.
[33] A.J. Karabelas, S.T. Mitrouli, M. Kostoglou, Scaling in reverse osmosis desalination plants: a perspective focusing on development of comprehensive simulation tools, Desalination 474 (2020) 114193.
[34] K.T. Huisman, B. Blankert, H. Horn, M. Wagner, J.S. Vrouwenvelder, S. Bucs, L. Fortunato, Noninvasive monitoring of fouling in membrane processes by optical coherence tomography: a review, J. Membr. Sci. 692 (2024) 122291.
[35] M. Wagner, D. Taherzadeh, C. Haisch, H. Horn, Investigation of the mesoscale structure and volumetric features of biofilms using optical coherence tomography, Biotechnol. Bioeng. 107 (2010) 844–853.
[36] S. West, M. Wagner, C. Engelke, H. Horn, Optical coherence tomography for the in situ three-dimensional visualization and quantification of feed spacer channel fouling in reverse osmosis membrane modules, J. Membr. Sci. 498 (2016) 345–352.
[37] L. Fortunato, S. Bucs, R.V. Linares, C. Cali, J.S. Vrouwenvelder, T. Leiknes, Spatially-resolved in-situ quantification of biofouling using optical coherence tomography (OCT) and 3D image analysis in a spacer filled channel, J. Membr. Sci. 524 (2017) 673–681.
[38] K.T. Huisman, N. Franco-Clavijo, J.S. Vrouwenvelder, B. Blankert, Improved quantitative evaluation of the fouling potential in spacer-filled membrane filtration channels through a biofouling index based on the relative pressure drop, J. Membr. Sci. 671 (2023) 121400.
[39] K.T. Huisman, Noninvasive monitoring of fouling in membrane processes by optical coherence tomography: a review, J. Membr. Sci. 671 (2023) 121400.
[40] J.-G. Lee, Y. Jang, L. Fortunato, S. Jeong, S. Lee, T. Leiknes, N. Ghaffour, An advanced online monitoring approach to study the scaling behavior in direct contact membrane distillation, J. Membr. Sci. 546 (2018) 50–60.
[41] J.S. Vrouwenvelder, J.A.M. van Paassen, L.P. Wessels, A.F. van Dam, S.M. Bakker, The membrane fouling simulator: a practical tool for fouling prediction and control, J. Membr. Sci. 281 (2006) 316–324.
[42] J.S. Vrouwenvelder, C. Hinrichs, W.G.J. Van der Meer, M.C.M. Van Loosdrecht, J. C. Kruithof, Pressure drop increase by biofilm accumulation in spiral wound RO and NF membrane systems: role of substrate concentration, flow velocity, substrate load and flow direction, Biofouling 25 (2009) 543–555.
[43] J.S. Vrouwenvelder, J. Buiter, M. Riviere, W.G.J. van der Meer, M.C.M. van Loosdrecht, J.C. Kruithof, Impact of flow regime on pressure drop increase and biomass accumulation and morphology in membrane systems, Water Res. 44 (2010) 689–702.
[44] A. Drak, K. Glucina, M. Busch, D. Hasson, J.-M. Laine, R. Semiat, Laboratory technique for predicting the scaling propensity of RO feed waters, Desalination (2000) 242.
[45] K.T. Huisman, L. Fortunato, J.S. Vrouwenvelder, B. Blankert, A clear view of biofouling in spacer filled membrane filtration channels: Integrating OCT and CT for improved visualization and localization, J. Membr. Sci. 697 (2024) 122573.
[46] K.T. Huisman, L. Fortunato, J.S. Vrouwenvelder, B. Blankert, Automated image processing algorithm for 3D OCT images of fouling in spacer-filled membrane filtration channels, MethodsX 13 (2024) 102871.
[47] C.W. Davies, 397. the extent of dissociation of salts in water. Part VIII. an equation for the mean ionic activity coefficient of an electrolyte in water, and a revision of the dissociation constants of some sulphates, J. Chem. Soc. (Resumed) (1938) 2093–2098.
[48] aqion, Hydrochemistry & Water Analysis, in, 2024.
[49] S. Cespedes, F.D. Martinez, F. Salto-Quintana, B. Blankert, C. Picioreanu, Three-dimensional concentration-polarization modeling of trace-ions in reverse osmosis, J. Membr. Sci. 693 (2024) 122349.
[50] J.W. Mullin, Crystallization (2001).
[51] S.G. Salinas-Rodriguez, J.C. Schippers, G.L. Amy, I.S. Kim, M.D. Kennedy, SWROAssessment and pretreatment of fouling and scaling, IWA Publishing, 2021.
[52] A. Sapalidis, Membrane desalination from nanoscale to real world applications, 2020.
[53] S.S. Bucs, R. Valladares Linares, M.C.M. van Loosdrecht, J.C. Kruithof, J. S. Vrouwenvelder, Impact of organic nutrient load on biomass accumulation, feed channel pressure drop increase and permeate flux decline in membrane systems, Water Res. 67 (2014) 227–242.
[54] A.I. Radu, L. Bergwerff, M.C.M. van Loosdrecht, C. Picioreanu, A two-dimensional mechanistic model for scaling in spiral wound membrane systems, Chem. Eng. J. 241 (2014) 77–91.
[55] P.M. Biesheuvel, S.B. Rutten, I.I. Ryzhkov, S. Porada, M. Elimelech, Theory for salt transport in charged reverse osmosis membranes: novel analytical equations for desalination performance and experimental validation, Desalination 557 (2023) 116580.
[56] B. Blankert, F.D. Martinez, J.S. Vrouwenvelder, C. Picioreanu, Solution-diffusion-electromigration approximation model (SDE-A) for strongly charged, weakly charged and effectively uncharged reverse osmosis membranes, J. Membr. Sci. 679 (2023) 121675.
[57] E.M.V. Hoek, M. Elimelech, Cake-enhanced concentration polarization: a new fouling mechanism for salt-rejecting membranes, Environ. Sci. Technol. 37 (2003) 5581–5588.
[58] H.I.o. Mineralogy, mindat.org, in.
[59] A. Rahardianto, W.-Y. Shih, R.-W. Lee, Y. Cohen, Diagnostic characterization of gypsum scale formation and control in RO membrane desalination of brackish water, J. Membr. Sci. 279 (2006) 655–668.
[60] W.-Y. Shih, A. Rahardianto, R.-W. Lee, Y. Cohen, Morphometric characterization of calcium sulfate dihydrate (gypsum) scale on reverse osmosis membranes, J. Membr. Sci. 252 (2005) 253–263.
[61] J. Gilron, D. Hasson, Calcium sulphate fouling of reverse osmosis membranes: flux decline mechanism, Chem. Eng. Sci. 42 (1987) 2351–2360.
[62] A.G. Pervov, Scale formation prognosis and cleaning procedure schedules in reverse osmosis systems operation, Desalination 83 (1991) 77–118.
[63] K. Popov, M. Oshchepkov, E. Afanas'eva, E. Koltinova, Y. Dikareva, H. Rönkkömäki, A new insight into the mechanism of the scale inhibition: DLS study of gypsum nucleation in presence of phosphonates using nanosilver dispersion as an internal light scattering intensity reference, Colloids Surf A Physicochem Eng Asp 560 (2019) 122–129.
[64] X. Liu, Heterogeneous nucleation or homogeneous nucleation? J. Chem. Phys. 112 (2000) 9949–9955.

[65] K. Popov, Y. Vainer, G. Silaev, V. Kuryakov, M. Trukhina, E. Koltinova, V. Trokhin, M. Oshchepkov, M. Butakova, A. Oshchepkov, Potential nano/microcenters of crystal nucleation in reagent-grade purity solvents and their differentiation by fluorescent-tagged antiscalant, Crystals (2024).
[66] J. Li, Z. Yin, Z. Ding, W. Liu, T. Wei, Q. Chen, W. Zhang, Homogeneous nucleation of Al(OH)3 crystals from supersaturated sodium aluminate solution investigated by in situ conductivity, Hydrometall. 163 (2016) 77–82.
[67] S. Halevy, E. Korin, J. Gilron, Kinetics of gypsum precipitation for designing interstage crystallizers for concentrate in high recovery reverse osmosis, Ind. Eng. Chem. Res. 52 (2013) 14647–14657.
[68] N. Dhakal, S.G. Salinas Rodriguez, J.C. Schippers, M.D. Kennedy, Induction time measurements in two brackish water reverse osmosis plants for calcium carbonate precipitation, Desalin. Water Treat. 53 (2015) 285–293.
[69] A. Jikazana, K. Garg, K. Le Corre Pidou, P. Campo, E.J. McAdam, The role of mixing on the kinetics of nucleation and crystal growth in membrane distillation crystallisation, Sep. Purif. Technol. 353 (2025) 128533.
[70] T. Rabizadeh, T.M. Stawski, D.J. Morgan, C.L. Peacock, L.G. Benning, The effects of inorganic additives on the nucleation and growth kinetics of calcium sulfate dihydrate crystals, Cryst. Growth Des. 17 (2017) 582–589.
[71] T. Waly, M.D. Kennedy, G.J. Witkamp, G. Amy, J.C. Schippers, Will calcium carbonate really scale in seawater reverse osmosis? Desalin. Water Treat. 5 (2009) 146–152.
[72] S.F.E. Boerlage, M.D. Kennedy, I. Bremere, G.J. Witkamp, J.P. Van der Hoek, J. C. Schippers, The scaling potential of barium sulphate in reverse osmosis systems, J. Membr. Sci. 197 (2002) 251–268.